



OPEN

A deep learning-based combination method of spatio-temporal prediction for regional mining surface subsidence

Yixin Xiao^{1,2}, Qiuxiang Tao^{1,2}✉, Leyin Hu³, Ruixiang Liu^{1,2} & Xuepeng Li^{1,2}

In coal mining areas, surface subsidence poses significant risks to human life and property. Fortunately, surface subsidence caused by coal mining can be monitored and predicted by using various methods, e.g., probability integral method and deep learning (DL) methods. Although DL methods show promise in predicting subsidence, they often lack accuracy due to insufficient consideration of spatial correlation and temporal nonlinearity. Considering this issue, we propose a novel DL-based approach for predicting mining surface subsidence. Our method employs K-means clustering to partition spatial data, allowing the application of a gate recurrent unit (GRU) model to capture nonlinear relationships in subsidence time series within each partition. Optimization using snake optimization (SO) further enhances model accuracy globally. Validation shows our method outperforms traditional Long Short-Term Memory (LSTM) and GRU models, achieving 99.1% of sample pixels with less than 8 mm absolute error.

Keywords Deep learning, GRU, Mining surface subsidence, Spatio-temporal prediction, Snake optimization algorithm

Coal mining has played a crucial role in China's economy, it has substantial reserves and high production. However, there are many geological disasters and environmental issues associated with coal mining. Subsidence, cracks¹, collapses, and other similar disasters have caused severe damage to the land resources and ecological environment in mining areas^{2–4}. Therefore, it is particularly important to establish accurate and effective prediction models and grasp the spatio-temporal evolution laws of surface subsidence in mining areas in advance.

Traditional methods for monitoring surface subsidence, such as leveling, global positioning system (GPS), and triangulation elevation measurement, have high monitoring accuracy⁵. These methods have drawbacks including high cost, heavy workload, and limited efficiency. Additionally, they cannot retrospectively capture the evolution of surface subsidence that has already occurred. To overcome these limitations, interferometric synthetic aperture radar (InSAR) technology has emerged, such as differential InSAR (DInSAR), small baseline subset InSAR (SBAS InSAR), and persistent scatterer InSAR (PS InSAR)^{6–11}. There are advantages like all-weather capability, high-precision, high spatio-temporal resolution, wide coverage, and low cost. A large number of research examples have shown that using InSAR to monitor mining surface subsidence is of great help in deeply understanding the mechanism and laws of surface subsidence in mining areas^{12–14}. Moreover, in recent years, with the increasingly mature application of InSAR in regional surface subsidence monitoring, combining InSAR with machine learning, deep learning, etc. to accurately predict regional surface subsidence has gradually become a new research hot spot^{15–20}.

In InSAR deformation prediction applications, convolutional neural network (CNN) methods to detect the slow deformation of volcanoes and forecast the short-term InSAR deformation maps in the early stage²¹. Nukala et al. presented a novel Recurrent Neural Network (RNN) method to forecast time series deformation maps based on Sentinel-1 images, which achieves good predictive performance²². The LSTM network resolves the problem that older variants of RNN can suffer from exploding and vanishing gradients limitations in learning long-range dependencies in the data. Some researchers established a time series InSAR deformation forecasting model

¹College of Geodesy and Geomatics, Shandong University of Science and Technology, Qingdao 266000, China. ²Demonstration Center for Experimental Surveying and Mapping Education, Shandong University of Science and Technology, Qingdao 266000, China. ³Center for Earthquake Monitoring and Researching, Beijing Earthquake Agency, Beijing 100000, China. ✉email: qiuxiangtao@163.com; skd992023@sdust.edu.cn

and indicated that the LSTM network has better prediction performance^{23,24}. Many methods of combination forecasting have also become hot topics among scholars^{25,26}. Muhammad Kamran et al. developed a decision intelligence-based predictive model for assessing the stability of hard rock pillars in underground engineering structures. The model integrates K-Nearest Neighbors with the Grey Wolf Optimization algorithm (KNN-GWO) to enhance accuracy in stability predictions²⁷. An innovative decision intelligence-driven predictive modeling approach integrating K-means clustering and random forest algorithms to accurately predict the air quality index (AQI) in surface coal mining, achieving a high prediction accuracy of 97%²⁸.

However, in the actual work of predicting surface subsidence in mining areas, it was found that existing deep learning prediction models for regional mining surface subsidence do not consider the spatial correlation and temporal nonlinear characteristics of subsidence, resulting in a lack of interpretability of prediction results^{29,30}. In addition, the prediction accuracy is significantly influenced by the parameters of the deep learning models, and it is necessary to continuously adjust the values of the parameters manually to achieve high-precision prediction, which is very complex to operate.

Therefore, this study considers the spatio-temporal correlation and temporal nonlinearity of mining surface subsidence, utilizes the obvious advantage of the GRU network model of deep learning in learning the nonlinear characteristics of mining surface subsidence time series, and proposes a combination method of spatio-temporal prediction for regional surface subsidence in mining area. This method utilizes a strategy of combining spatial partitioning and local modeling to weaken the impact of spatial differences, utilizes the GRU network model of deep learning to capture the nonlinearity of surface subsidence in mining areas, utilizes an intelligent optimization algorithm (snake optimization algorithm) to globally optimize the parameters of the GRU model and adaptively determine the optimal parameters, avoiding the tedious and random nature of manual parameter adjustment with strong adaptability and higher accuracy, the final objective was to achieve high-precision regional surface subsidence prediction in mining areas.

Materials and methods

Study area

A mining area in Heze City, Shandong Province, China was selected as the study area, its geographical location and scope were shown in Fig. 1. This area belongs to the Yellow River alluvial plain, with a flat terrain, a ground elevation of +41 m to +46 m, a natural terrain slope of 0.2‰, and a total area of approximately 259 km². The main coal types are fat coal, one-third coking coal, and gas coal. The depth, thickness and date of coal mining is 938 m, 6.8 m and since 2006, respectively. The overlying features include mostly farmland with common crops such as wheat, corn, and sweet potato, along with economic crops such as soybean, cotton, and vegetables. Furthermore, the industrial, construction, animal husbandry, and tertiary industries are relatively developed. The above natural conditions and the coal mining have caused serious surface subsidence problems in this study area, addressing the contradiction between underground coal mining and surface protection is an important work to achieve efficient and civilized production, and it is particularly important to conduct temporal monitoring and prediction.

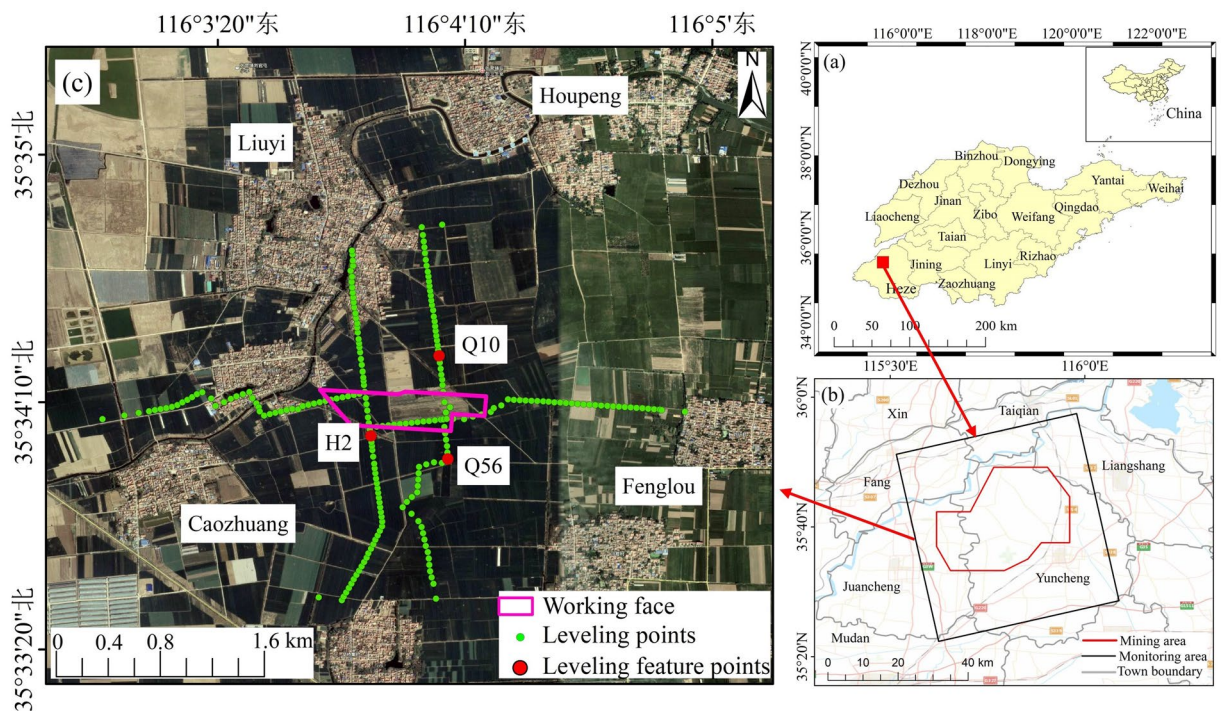


Figure 1. Location and scope of the study area: (a) location of the study area; (b) enlarged image and scope of the study area; and (c) location and distribution of the leveling points.

In addition, the leveling monitoring surface subsidence values of 211 leveling points were compiled to compare, analyse, and verify the accuracy and reliability of the SBAS InSAR monitoring surface subsidence time series. The distribution and extent of the 211 leveling points were shown in Fig. 1c. The leveling data was measured according to the fourth-order leveling survey rules and using the American Trimble DiNi03 electronic level, and the allowable closing error was $20\sqrt{L}$ mm (L is the length of the leveling line in km).

Accuracy analysis of SBAS InSAR

The Sentinel-1 satellite constellation is an earth observation plan of the European Space Agency Copernicus Program (Global Monitoring for Environment and Security) and is composed of Sentinel-1 A satellite and Sentinel-1 B satellite. The two satellites were successfully launched on April 3, 2014, and April 25, 2016, respectively. The two satellites can observe ground with all-weather and continuous radar imaging since they carry a C-band synthetic aperture radar and fly at an on-orbit altitude of 693 km. More importantly, Sentinel-1 A and B can work in different modes, e.g., single and dual polarization work modes, with excellent timeliness and reliability³¹. In this study, 66 Sentinel-1A SAR images from January 10, 2019, to April 5, 2021 were selected and processed using SBAS InSAR to obtain the mining surface subsidence time series of the study area. In detail, due to high accuracy and less time cost, the GAMMA software was used to calculate surface subsidence based on SBAS, with temporal baseline of 365 days, max normal baseline of 45% and unwrapping coherence threshold of 0.3 for first unwrapping and 0.2 for the second. In order to obtain a uniformly distributed time series of mining surface subsidence and minimize the surface subsidence prediction error, linear interpolation was performed when encountering subsidence values with a 24 day interval (January 10, 2019 to February 3, 2019, February 3, 2019 to February 27, 2019, August 26, 2019 to September 19, 2019). The resulting time series comprised subsidence values over 69 periods, each period as 12-days. Figure 2 shows the surface subsidence time series of six periods.

The leveling monitoring covered 19 periods from January 26, 2019, to April 4, 2021, with data from 211 leveling points. The SBAS InSAR monitoring spanned 69 periods from January 10, 2019, to April 5, 2021. To align the data, a piecewise linear interpolation was applied to the leveling results to match the SBAS InSAR data. The difference between the two monitoring methods, i.e., leveling monitoring and SBAS InSAR was then calculated for analysis. Figures 4 and 5 compare surface subsidence results from leveling and SBAS InSAR. Figure 4 displays surface subsidence curves for points H2, Q56, and Q10 over 69 dates from January 10, 2019, to April 5, 2021. Figure 5 shows histogram plots of surface subsidence values at 211 leveling points across three monitoring periods.

Figures 3 and 4 shows that leveling and SBAS InSAR could successfully monitor the continuous surface subsidence during the period from January 10, 2019, to April 5, 2021, and the surface subsidence time series in mining area exhibited obvious nonlinear characteristics.

For example, on leveling point H2 in Fig. 3a, during the first 16 monitoring periods, the subsidence values were similar and highly correlated. From the 17th to 29th monitoring periods, subsidence continued but at different rates between leveling and SBAS InSAR. During the 30th to 41st periods, leveling showed a rapid subsidence with an increased velocity, while SBAS InSAR also showed rapid subsidence, but with a lower velocity. From the 41st to 69th periods, leveling and SBAS InSAR both showed slowing down of surface subsidence, with SBAS InSAR having higher velocity than leveling. In Fig. 4, the histograms of mining surface subsidence values monitored by leveling and SBAS InSAR on 211 leveling points exhibited similar shapes. This suggested that the mining surface subsidence values of leveling and SBAS InSAR monitoring were relatively close to each other.

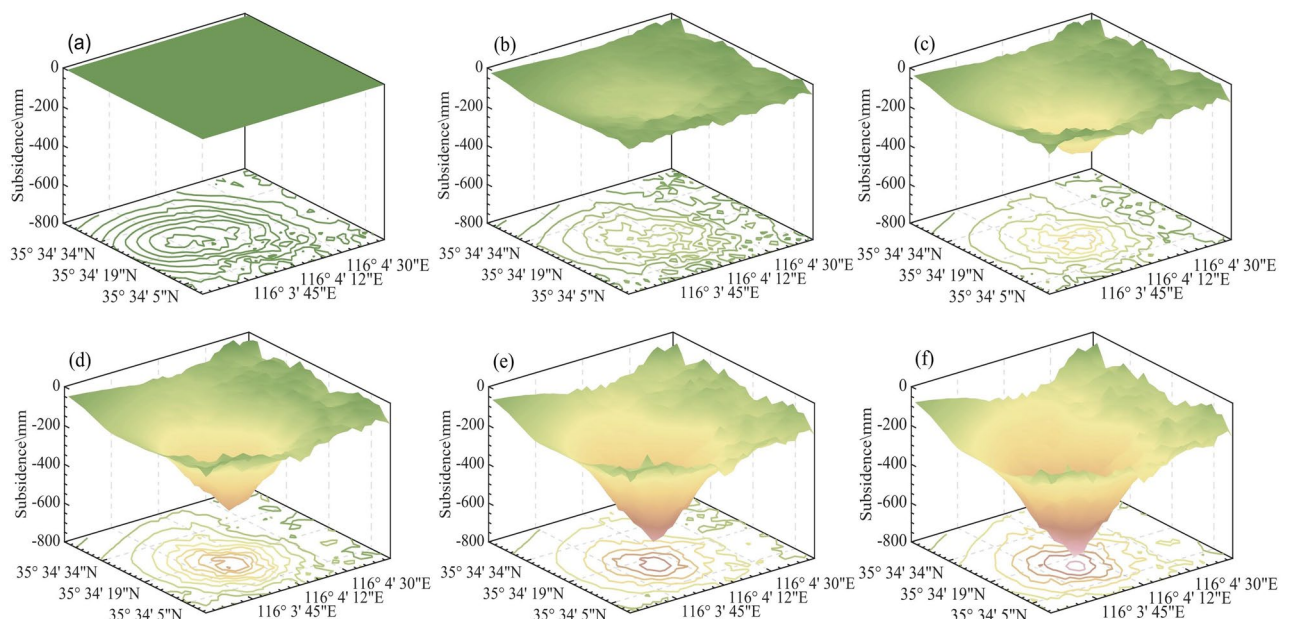


Figure 2. Mining surface subsidence time series of six periods monitored by SBAS InSAR: (a) January 10, 2019–March 11, 2019, (b) January 10, 2019–July 9, 2019, (c) January 10, 2019–November 18, 2021, (d) January 10, 2019–March 17, 2020, (e) January 10, 2019–September 13, 2020, and (f) January 10, 2019–April 5, 2021.

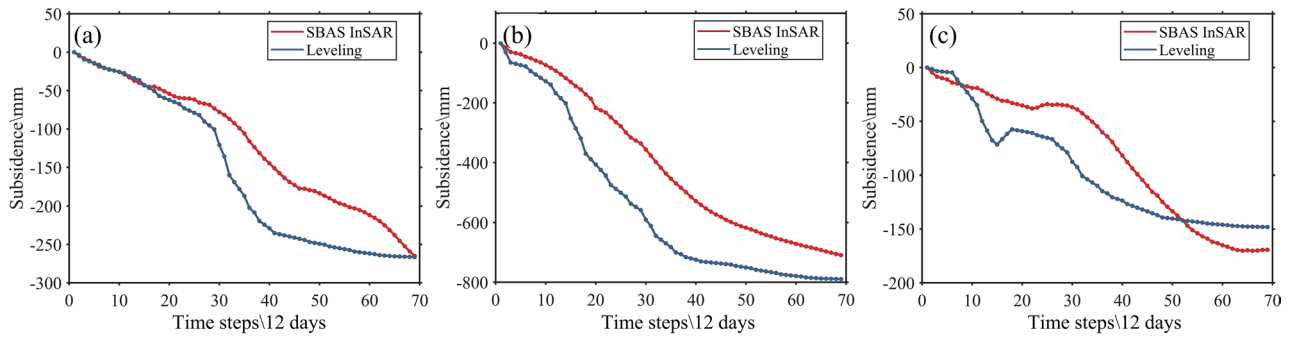


Figure 3. Curves of mining surface subsidence time series on three leveling points: (a) H2, (b) Q10, (c) Q56.

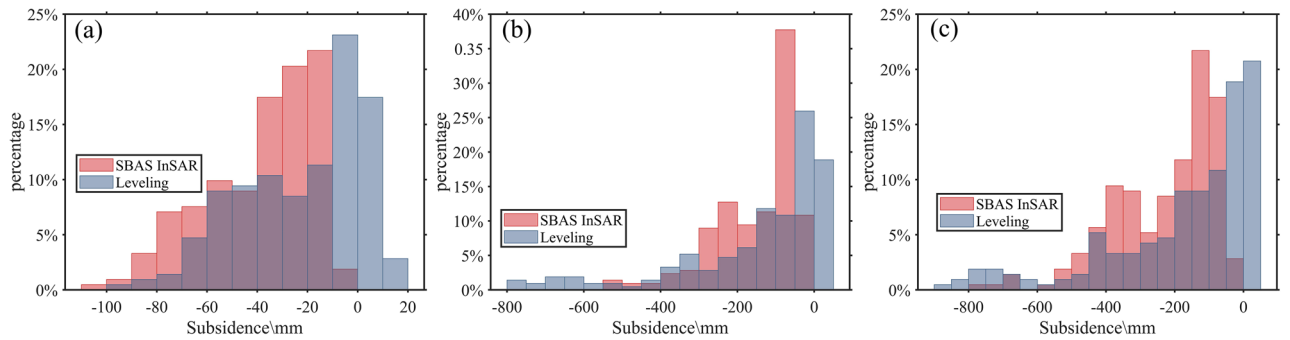


Figure 4. Histogram of mining surface subsidence values on 211 leveling points: (a) January 10, 2019–May 5, 2019, (b) January 10, 2019–April 22, 2020, and (c) January 10, 2019–April 5, 2021.

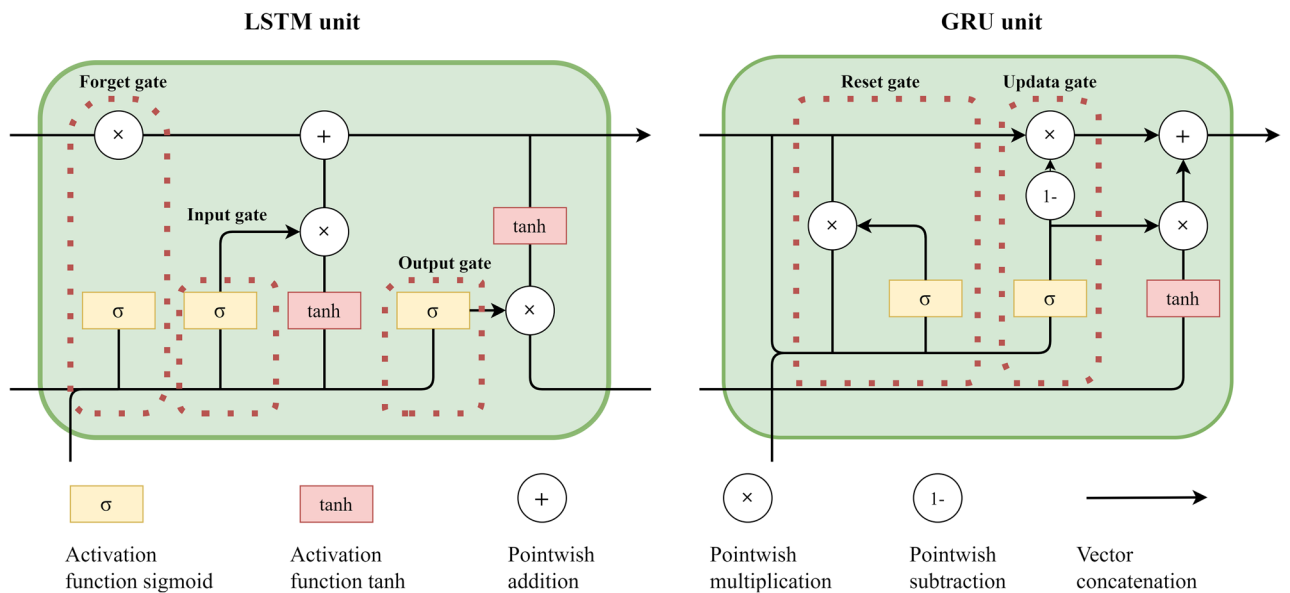


Figure 5. Basic structures of LSTM and GRU neural networks.

Overall, the analysis and comparison of the mining surface subsidence of SBAS InSAR and leveling monitoring demonstrated the consistency and accuracy of the SBAS InSAR monitoring, the spatio-temporal distribution of surface subsidence in mining areas monitored by SBAS InSAR was reliable.

Spatio-temporal distance and K-means clustering

This study used a combination strategy of spatio-temporal distance and K-means clustering algorithm (hereinafter referred to as SDK) to determine the spatial partitions of the mining surface subsidence time series.

This method comprehensively considers and describes the spatio-temporal correlation and similarity of surface subsidence time series between adjacent pixels, and obtains more reasonable partitioning results.

Firstly, the spatio-temporal distance between the nearest neighboring pixels is calculated. The spatio-temporal distance refers to the weighted sum of temporal and spatial distances between the two pixels.

Assuming two pixels are P_i and P_j , with longitude and latitude coordinates of (lon_i, lat_i) and (lon_j, lat_j) , respectively, and the average values of the surface subsidence time series monitored by SBAS InSAR are t_i and t_j , the spatio-temporal distance $d_{i,j}$ between them can be calculated using the following equation:

$$d_{i,j} = \omega_s \sqrt{\left(\frac{lon_i - lon_j}{\alpha}\right)^2 + \left(\frac{lat_i - lat_j}{\beta}\right)^2} + \omega_t \gamma |t_i - t_j|, \quad (1)$$

where ω_s and ω_t refer to the weights of temporal and spatial distances, α and β refer to the coefficients for scaling latitude and longitude, γ refers to the coefficient for scaling temporal distance. In this study, ω_s and ω_t were set to 0.5, α , β , and γ were set to 1.

Then, K-means clustering is performed based on the above spatio-temporal distance. K-means clustering is widely recognized as an effective clustering method^{32,33}. The algorithm first randomly selects k pixels as cluster centers, where k represents the desired number of clusters and can be determined by the following elbow method^{34–36}. Subsequently, calculates the spatio-temporal distance between each pixel and each initial cluster center. Based on the shortest distance, assigns each pixel to the nearest cluster center to form initial clusters. Recalculates the cluster center of each initial cluster based on the existing pixels in that cluster, and determines the new cluster centers. Subsequently, calculates the spatio-temporal distance between each pixel and each new cluster center. Based on the shortest distance again, assigns each pixel to the nearest cluster center to form new clusters. This iterative process will continue until one of the following termination conditions is met: (1) No (or the minimum number) pixels are reassigned to different clusters, (2) no (or the minimum number) cluster centers change again, and (3) the sum of squared errors (SSE) is minimized. In this study, the third condition was selected as the iterative termination condition, and the objective function of K-means clustering was defined as³⁷:

$$\min (SSE) = \min \left(\sum_{i=1}^k \sum_{x \in C_i} (D_i - x)^2 \right), \quad (2)$$

where C_i refers to the i th cluster, D_i refers to the cluster center of C_i , x refers to the pixels of C_i .

LSTM and GRU

LSTM and GRU are two types of recurrent neural networks^{38,39}. The main difference between the two lies in the different gating mechanisms. LSTM uses three gates to control the information flow, namely input gate, forget gate, and output gate. The input gate and forget gate respectively control whether new input data and previous memory are written, and the output gate controls whether the output values should be passed to the next layer⁴⁰. GRU only uses two gates, namely reset gate and update gate. The update gate controls the degree that the previous state information is retained in the current state, while the reset gate is used to determine how the current state is combined with previous memory. Compared to LSTM, GRU is simpler, fewer gating structures reduce the risk of over fitting, fewer parameters reduce the computational complexity, and improve operational efficiency. Overall, the advantages of the GRU lie in its simplicity, faster training speed and computational efficiency, and higher generalization ability. Figure 5 illustrates the basic structures of LSTM and GRU neural networks.

Snake optimization algorithm

The number of neurons, learning rate, dropout rate, and batch size of training samples are key parameters that affect the performance of the GRU network model. A novel meta-heuristic optimization algorithm called snake optimization algorithm was used to globally optimize these parameters⁴¹. It simulates the feeding and breeding behaviors of a snake to reduce the average prediction error and achieve efficient parameter combination optimization, with numerous advantages, e.g., faster compute, higher precision and robustness^{42,43}. It is widely used in the fields of machine learning and deep learning. its process involves the following steps⁴⁴:

- (1) Parameter definition and population initialization: Determine the parameters that need to be optimized. In this study, the parameters were the number of neurons, learning rate, dropout rate, and batch_size of GRU. Additionally, apply the SO algorithm to generate an initial set of positions (parameter combinations) for the GRU model, with each position corresponding to an individual.
- (2) Fitness calculation: Calculate the RMSE of the model's predicted subsidence values. Lower RMSE values indicate better fitness. The fitness function can be mathematically expressed as follows^{45–47}:

$$RMSE = \sqrt{\frac{1}{n} \sum_{i=1}^n (\hat{y}_i - y_i)^2}, \quad (3)$$

where n denotes the number of samples, y_i denotes the actual subsidence values, and \hat{y}_i denotes the predicted values.

- (3) Iterative optimization and model training: Use SO algorithm to simulate the feeding and breeding behaviors of a snake and adjust its position to find the parameters combination with the best fitness value. Obtain the

optimal combination of network model parameters, and use these optimal parameters to train the GRU prediction model.

Deep learning-based combination method of spatio-temporal prediction

To address the issues of existing models not taking into account the spatio-temporal correlation this study proposed spatio-temporal prediction method (Fig. 6) for regional mining surface subsidence can adaptively determine the optimal parameters, avoiding the tedious and random manual parameter adjustment, and ensuring that the model has strong adaptability and higher accuracy. The implementation of this method mainly involves the following three steps: Firstly, the SKD method is used to divide the surface subsidence time series into a group of partitions. Then, learn different subsidence patterns and construct local models within each partition. Finally, use the well-trained model to make short-term prediction of future regional mining surface subsidence.

Results

Pretreatment

The experimental data was the SBAS InSAR monitoring surface subsidence time series of 30,965 pixels in the study area, with subsidence values on 69 dates (with an interval of 12 days) from January 10, 2019 to April 5, 2021. The preceding section above provides a detailed description and accuracy verification of the data.

In order to better utilize the spatial correlation characteristics of surface subsidence time series in the mining area, the study area should be firstly divided into several partitions by the SDK strategy.

As shown in Fig. 7a, there was a distinct inflection point (i.e. elbow point) when the number of clusters was “3”. Therefore, we chose to cluster the study area into three partitions. The partition results of k-means clustering are shown in Fig. 8a, partition1 had 3718 sample pixels, partition2 had 9056 sample pixels, and partition3 had 18,191 sample pixels. Comparing Fig. 8a,b, it was found that each partition not only aggregated time series with similar subsidence characteristics, but also highly matched the spatial distribution of surface subsidence in the mining area, further verifying the reliability of the SDK strategy.

In order to enable the GRU network model to accurately learn these nonlinear subsidence patterns and increase the number of training samples, assuming that the surface subsidence time series of sample pixels within each partition have the same subsidence pattern, and their subsidence velocities are roughly the same within L time intervals, so L can be called the optimal sample input length^{38,39}. If the surface subsidence time series of each sample pixel is denoted as $D_m = \{d_1, d_2, \dots, d_m\}$ (m equals 69 in this study), there is $2 \leq L < m$, and the surface subsidence time series will be decomposed into $m - L + 1$ subsidence time series, which can be expressed as $\{D_1, D_2, \dots, D_{m-L+1}\}$ and $D_i = \{d_i, d_{i+1}, \dots, d_{i+L-1}\}$ ^{38,39}.

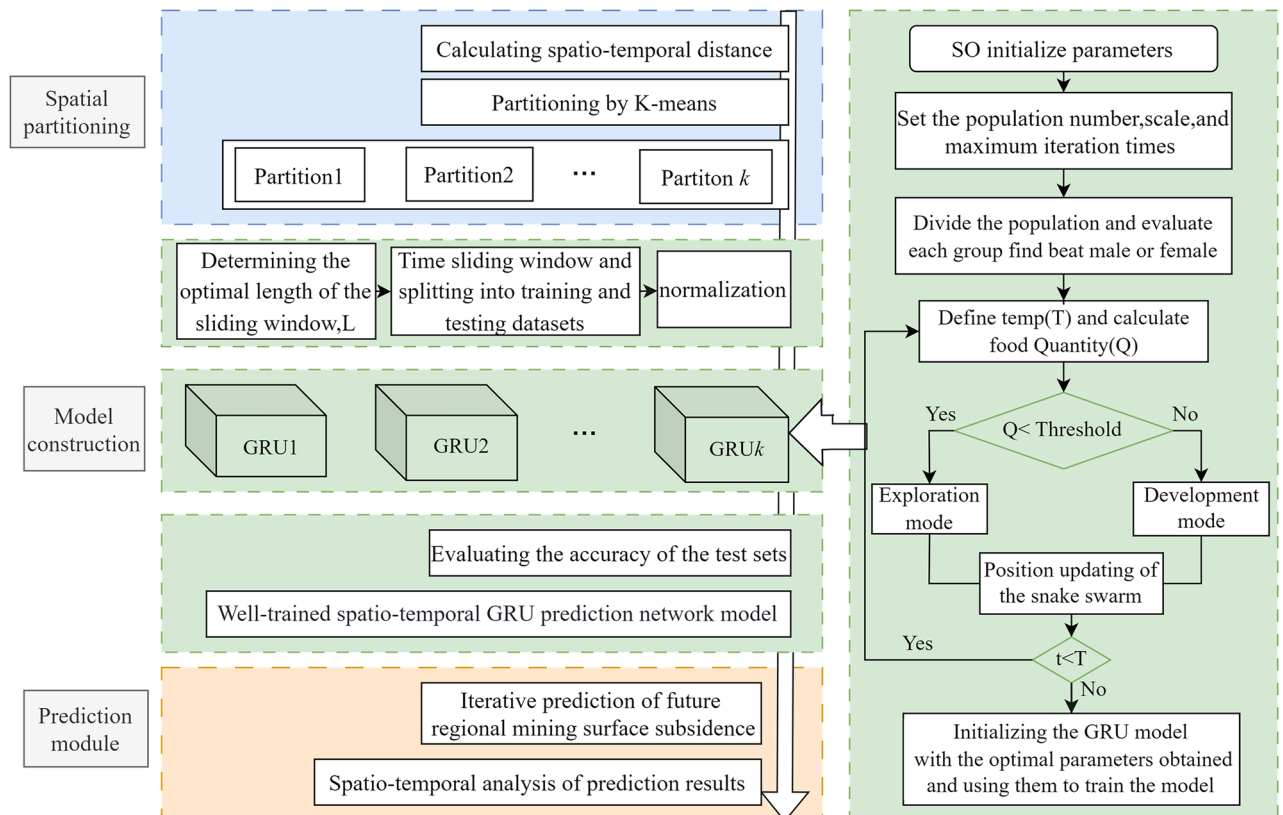


Figure 6. Spatio-temporal prediction combination model and data processing flow of regional mining surface subsidence based on deep learning.

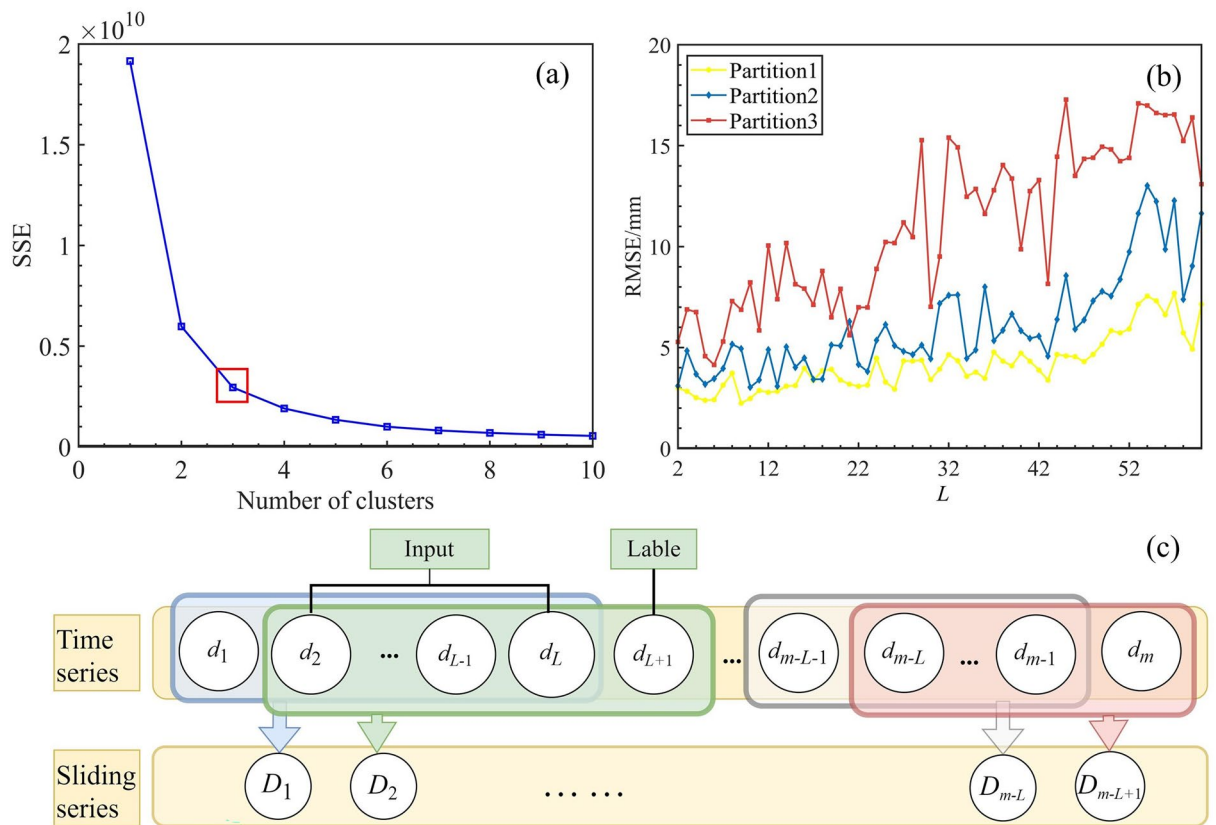


Figure 7. (a) Relationship curve between SSE and number of clusters. (b) Relationship curves between sample input length L and RMSE of the predicted subsidence value of the testing set sample labels within each partition. (c) Decomposition process of the surface subsidence time series.

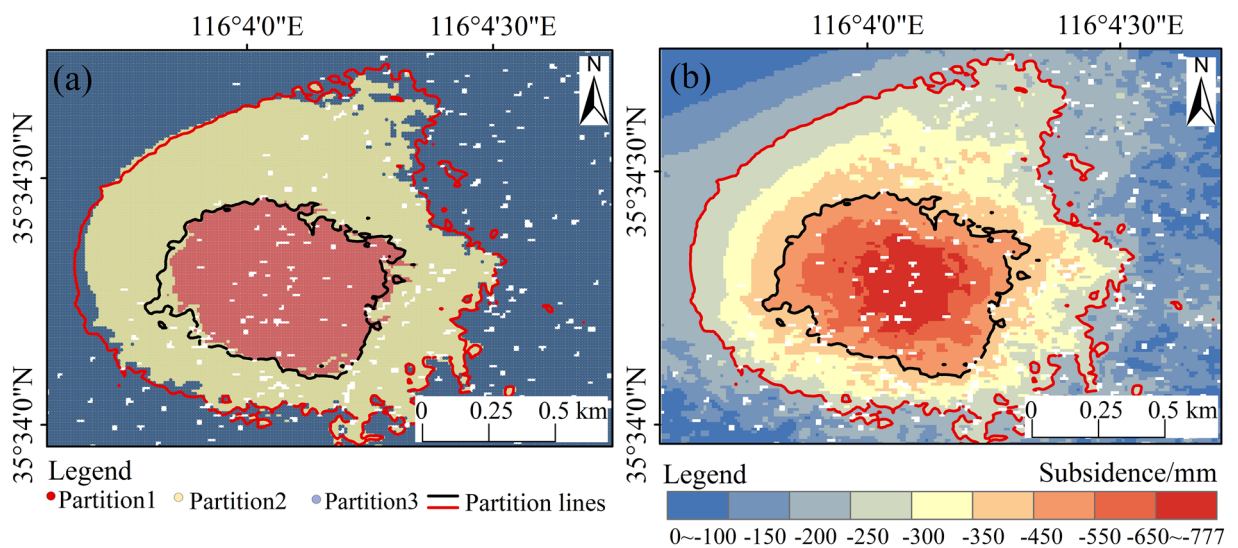


Figure 8. Results of spatial partitioning: (a) three partitions divided by the SDK strategy, and (b) final cumulative surface subsidence in the study area monitored by SBAS InSAR on April 5, 2021.

In Fig. 7c, for each surface subsidence time series, the first $L - 1$ values $\{d_i, d_{i+1}, \dots, d_{i+L-2}\}$ and the last value d_{i+L-1} are used as the sample inputs and labels for training GRU network model, respectively. For each sliding series, the first 80% and last 20% of $\{D_1, D_2, \dots, D_{m-L+1}\}$ of each sample pixel are used as the training and testing sets for the GRU network model, respectively.

As shown in Fig. 7b, when the sample input lengths L in partitions 1, 2, and 3 were 8, 14, and 6, respectively, the RMSE of predicted surface subsidence values on the sample labels of the testing set was the smallest. Therefore, the optimal sample input lengths for these three partitions should be 8, 14, and 6.

Finally, the training and testing series were standardized using the z-score to eliminate the influence of magnitude order of the surface subsidence time series on the training results⁴⁸. The specific data standardization method is the following equation

$$Z = (X - \mu) / \sigma, \quad (4)$$

where X refers to the surface subsidence time series, μ and σ refer to the average value and the standard deviation of the time series, respectively.

The standardized surface subsidence time series was recorded as $\{Z_1, Z_2, \dots, Z_{m-L+1}\}$ and $Z_i = \{z_i, z_{i+1}, \dots, z_{i+L-1}\} i = 1, 2, \dots, m - L + 1$.

Spatio-temporal analysis of surface subsidence

In each partition, the first 80% of standardized time series $\{Z_1, Z_2, \dots, Z_{m-L+1}\}$ of each sample pixel was used as the training set to train GRU network model, and the last 20% was used as the testing set to test GRU network model.

In the GRU network model training, many network parameters are involved, among which the number of neurons in the GRU hidden layer, learning rate, dropout rate, and batch_size of training samples are the most critical. In this study, the SO algorithm was used to globally optimize these four parameters, and use these optimal parameters to train the GRU network model.

As shown in Fig. 9, within the three partitions, the coefficient of determination were all as high as 0.99. This indicated that the predicted surface subsidence values within each partition were significantly positively correlated with the SBAS InSAR monitoring values, indicating that the combination prediction model trained in this experimentation was effective.

To further validate the proposed combination prediction method's validity and overall effectiveness in predicting regional mining surface subsidence, the LSTM and GRU were also employed to predict the surface subsidence values in the study area without dividing spatial partitions and parameters optimization. The first 80% of the standardized time series $\{Z_1, Z_2, \dots, Z_{m-L+1}\}$ of each sample pixel was used as the training set for model training, and the last 20% was used as the testing set for model testing. The critical parameters used for training the LSTM and GRU network models are as follows: number of neurons—128, learning rate—0.001, dropout rate—0.20, batch size—4096.

As shown in Fig. 10a–c, the surface subsidence distribution and values predicted by the three methods in the mining area were very consistent with the results of SBAS InSAR monitoring. The prediction results of the three methods were reliable. However, as shown in Fig. 10d–f, the prediction accuracy of our method was significantly higher than the other two methods. Specifically, in the prediction results of our method, there were 30,686 sample points (99.1% of all sample pixels) with an absolute error of less than 8 mm. In the prediction results of GRU and LSTM methods, there were 29,975 sample points (96.8% of all sample pixels) and 29,757 sample points (96.1% of all sample pixels) with an absolute error of less than 8 mm, respectively. The prediction accuracy of our method was higher than that of LSTM and GRU.

Spatio-temporal prediction of surface subsidence

Assuming the input data set is X and the prediction result is Y , use the cyclic prediction mode to predict the subsidence value of the $(L + 1)$ st moment based on the subsidence values of the first L moments, and add the predicted subsidence value of the $(L + 1)$ st moment to the input data set to form a new X , and then the new value of the $(L + 2)$ th moment is predicted.

The combination of cyclic prediction mode and well-trained spatio-temporal GRU network model was used to make short-term surface subsidence prediction in regional mining areas for 15 time periods within 180 days (April 5, 2021 to October 2, 2021), with an equal time interval of 12 days. Figure 11 shows the regional mining

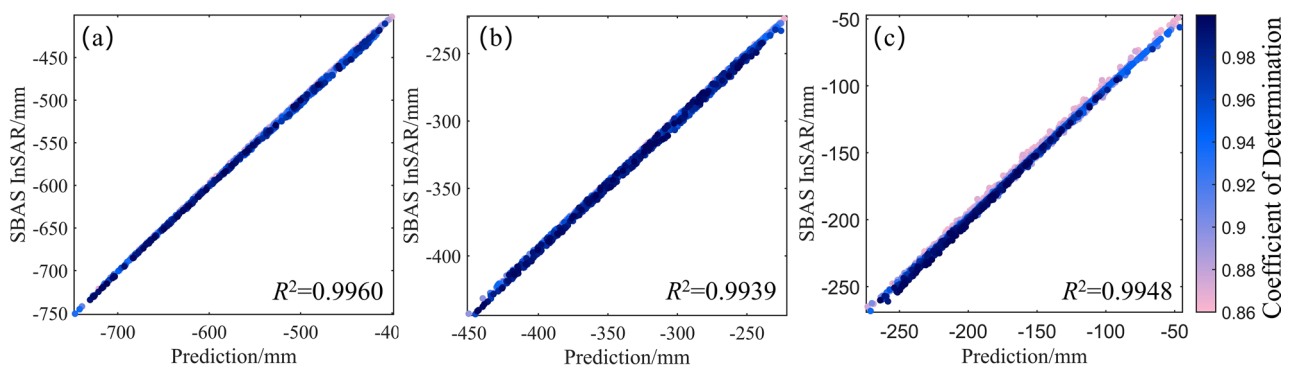


Figure 9. Relationship and coefficient of determination between the predicting and SBAS InSAR monitoring surface subsidence values on the last day of the testing set (i.e. April 5, 2021): (a) Partition1, (b) Partition2, and (c) Partition3.

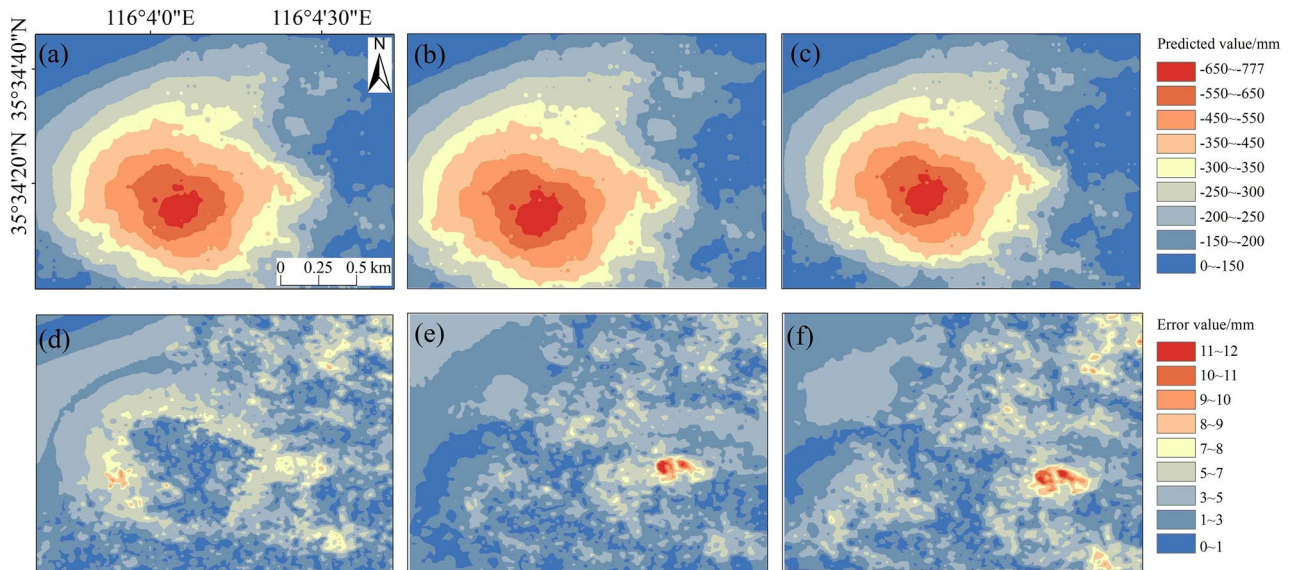


Figure 10. Regional mining surface subsidence and their absolute error predicted by the combined prediction method, GRU, and LSTM on the last day of the testing set (i.e. April 5, 2021): (a) combination prediction method's predicted subsidence, (b) GRU's predicted subsidence, (c) LSTM's predicted subsidence, (d) combination prediction method's prediction error, (e) GRU's prediction error, and (f) LSTM's prediction error.

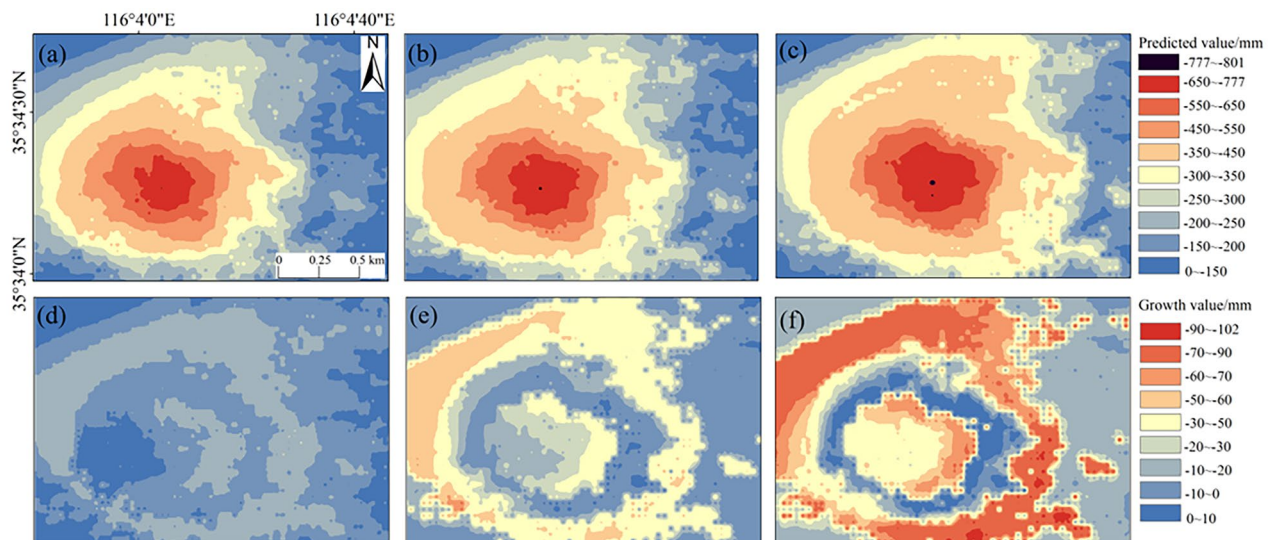


Figure 11. Predicted regional surface subsidence and their growth values within 180 days in the mining area: (a) January 10, 2019–April 17, 2021, (b) January 10, 2019–June 28, 2021, (c) January 10, 2019–October 2, 2021, (d) April 5, 2021–April 17, 2021, (e) April 5, 2021–June 28, 2021, and (f) April 5, 2021–October 2, 2021.

surface subsidence and their growth values during three periods predicted by the presented deep learning-based combination prediction method.

As shown in Fig. 11a–f, the mining surface subsidence in the study area would gradually increase in the next 6 months, and the maximum cumulative subsidence value at the subsidence center would reach -801 mm. The range of surface subsidence would continuously expand, and the subsidence basin obviously expand too. The surface subsidence trend at the center of the basin would become gentle, while the subsidence at the edges would become more severe.

As shown in Fig. 12a–c, the predicted surface subsidence time series after April 5, 2021 were very consistent with the previous subsidence trend shown in the SBAS InSAR monitoring results. The maximum cumulative subsidence value of the three leveling feature points H2, Q10, and Q56 would reach -327 mm, -747 mm, and -188 mm in the next six months, respectively. On the leveling points Q10 and Q56, the surface showed a sustained and slow downward trend in the next 6 months, while on H2, the surface showed a trend of first continuous decline and then gradually stabilizing in the next 6 months.

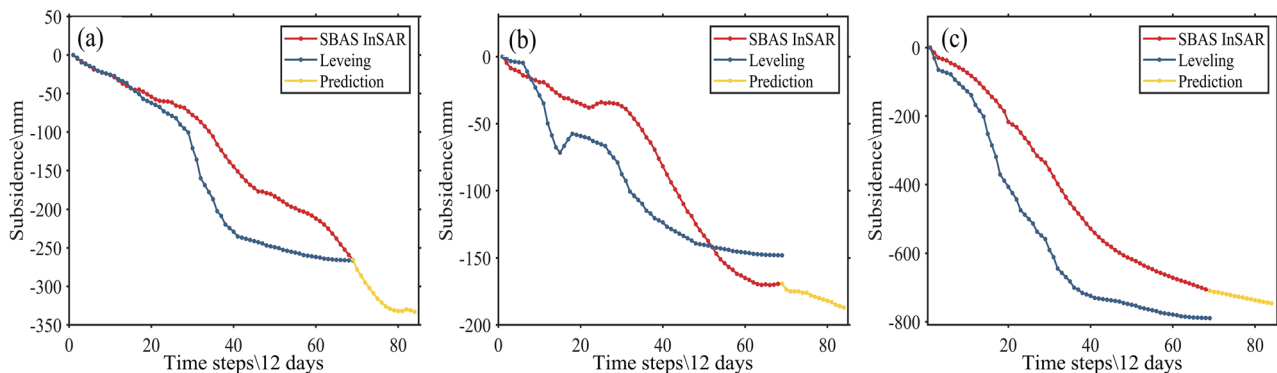


Figure 12. Predicted surface subsidence time series on the three leveling points: (a) H2, (b) Q10, and (c) Q56.

Discussion

Comparison experiment

To validate the prediction performance of our combination prediction method, we quantitatively compared it with three famous models: MLR, RNN, and SVR. Prediction errors, e.g. MAE RMSE R^2 , were used as evaluation metrics, with all methods using the same data source. As shown in Table 1, our combined method outperforms the other algorithms, as evidenced by the highest R^2 (0.9918) and lowest RMSE (2.35).

Research limitations

While the feasibility and high accuracy of our prediction algorithm have been validated in coal, some shortcomings of our combination strategy need to be discussed and addressed.

- (1) The above comparison experiments show that the combination method proposed in this study has the highest prediction accuracy. However, our algorithm is limited by data processing in terms of complex data pre-processing. Only using these data pre-processing approaches can ensure the excellent accuracy of our algorithm. The following work should discuss simplifying data processing and ensuring high accuracy.
- (2) The GRU model we used for time series prediction in this study can be improved. Like another DL-based model, e.g., LSTM, the GRU model relies on samples in terms of quantity and quality to improve its performance in predicting surface subsidence. Therefore, obtaining enough data at a low cost is an issue that needs to be addressed.
- (3) Additionally, the GRU model shows high accuracy and robustness in the short term but performs worse in predicting surface subsidence in the long term, which may be attributed to its construction.
- (4) Our algorithm assumed that the surrounding geologic environment (e.g., sediment thickness and land use type) would not change significantly over the study period, and we focused on predicting surface subsidence at a slow speed. Therefore, our algorithm is not applied for prediction of transient scenarios (e.g. landslides and earthquakes).

Conclusion

In regions affected by coal mining, surface subsidence poses significant risks to human life and property. Therefore, it is essential to establish accurate and effective prediction models and grasp the spatio-temporal evolution laws of surface subsidence in mining areas in advance. In this study, the spatio-temporal correlation and temporal nonlinear characteristics of mining surface subsidence were considered, and a DL-based combination method of spatio-temporal prediction for regional mining surface subsidence was proposed. Consequently, high-precision regional surface subsidence prediction of a mining area in Heze City, Shandong Province, China, was obtained based on the SBAS InSAR monitoring surface subsidence time series. The main conclusions are as follows:

Model	MAE/mm	RMSE/mm	R^2	Absolute error of less than 8 mm (%)
MLR	5.16	5.57	0.9589	92.7
SVR	4.97	5.32	0.9691	93.2
RNN	3.15	3.47	0.9815	94.3
LSTM	2.49	2.88	0.9866	96.1
GRU	2.35	2.71	0.9874	96.8
Combination method	2.04	2.35	0.9918	99.1

Table 1. Comparison of experimental results of different prediction model.

- (1) To considering spatio-temporal relationship of surface subsidence in mining areas, the three partitions obtained by spatio-temporal distance, K-means clustering algorithm, and elbow method, which were highly consistent with the spatial distribution of SBAS InSAR monitored surface subsidence. Strengths and flexibility of the partitioning method is highlighted by the partitioning results
- (2) Due to that the surface subsidence time series in mining areas exhibited obvious nonlinear characteristics, the optimal sample input length L of each partition was determined based on the minimum RMSE. The subsidence time series of each sample pixel was then decomposed into several subsidence time series at L time intervals to construct the training and testing sets of the GRU network model. The sample sets established not only increase the number of training and testing set, but also enable GRU network model to more accurately learn the nonlinear surface subsidence patterns in mining areas. Consequently, the distribution and values of predicted surface subsidence were reliable and closely consistent with the monitoring results of SBAS InSAR.
- (3) Using RMSE as the fitness, the SO algorithm was used to globally optimize the number of neurons, learning rate, dropout rate, and batchsize of training samples to train the GRU network model. Subsequently, a well-trained and optimal GRU prediction network model was constructed. By using this model, high-precision prediction of surface subsidence in regional mining areas can be obtained. This adaptive method of determining the optimal parameters eliminated tedious and random manual parameter adjustments, ensuring prediction model with strong adaptability and high accuracy.
- (4) Compared to LSTM and existed GRU model, our DL-based combination method of spatio-temporal prediction for regional mining surface subsidence has higher prediction accuracy. The predicted surface subsidence time series in the next 6 months exhibited good agreement with the subsidence trend observed in the early SBAS InSAR monitoring results.

Overall, this study expands the applicability of GRU network models in the field of surface subsidence prediction and the application scope of deep learning techniques, which can help accurate prediction of surface subsidence, especially in coal.

Data availability

The remote sensing and DEM datasets supporting the results of this study are publicly available through ASF Data Search (<https://search.asf.alaska.edu>) as well as Earth Explorer (<https://earthexplorer.usgs.gov>). Reference data are available from the corresponding author upon reasonable request.

Received: 28 February 2024; Accepted: 13 August 2024

Published online: 19 August 2024

References

1. Huang, B. *et al.* The effect of overlying rock fracture and stress path evolution in steeply dipping and large mining height stope. *Geomech. Geophys. Geo-Energy Geo-Resour.* **10**(1), 1–9 (2024).
2. Whittaker, B. N. & Reddish, D. J. *Subsidence: Occurrence, Prediction and Control* (Elsevier, 1989).
3. Conway, B. D. Land subsidence and earth fissures in south-central and southern Arizona, USA. *Hydrogeol. J.* **24**, 649–655. <https://doi.org/10.1007/s10040-015-1329-z> (2016).
4. Gill, J. C. & Malamud, B. D. Anthropogenic processes, natural hazards, and interactions in a multi-hazard framework. *Earth Sci. Rev.* **166**, 246–269. <https://doi.org/10.1016/j.earscirev.2017.01.002> (2017).
5. Yong-qin, G. Application of GPS in mining subsidence monitoring. *Coal Technol.* **32**, 124 (2013).
6. Li, S., Xu, W. & Li, Z. Review of the SBAS InSAR time-series algorithms, applications, and challenges. *Geodesy Geodyn.* **13**, 114–126. <https://doi.org/10.1016/j.geog.2021.09.007> (2022).
7. Pawluszek-Filipiak, K. & Borkowski, A. Integration of DInSAR and SBAS techniques to determine mining-related deformations using sentinel-1 data: The case study of Rydułtowy Mine in Poland. *Remote Sens.* **12**, 242 (2020).
8. Rosi, A. *et al.* The new landslide inventory of Tuscany (Italy) updated with PS-InSAR: Geomorphological features and landslide distribution. *Landslides* **15**, 5–19. <https://doi.org/10.1007/s10346-017-0861-4> (2018).
9. Jianjun, Z. H., Zhiwei, L. I. & Jun, H. U. Research progress and methods of InSAR for deformation monitoring. *Acta Geodaet. Cartogr. Sin.* **46**, 1717–1733. <https://doi.org/10.11947/j.AGCS.2017.20170350> (2017).
10. Biggs, J. & Wright, T. J. How satellite InSAR has grown from opportunistic science to routine monitoring over the last decade. *Nat. Commun.* **11**, 3863. <https://doi.org/10.1038/s41467-020-17587-6> (2020).
11. Hooper, A. A multi-temporal InSAR method incorporating both persistent scatterer and small baseline approaches. *Geophys. Res. Lett.* **35**, 654. <https://doi.org/10.1029/2008GL034654> (2008).
12. Dong, S., Samsonov, S., Yin, H., Ye, S. & Cao, Y. Time-series analysis of subsidence associated with rapid urbanization in Shanghai, China measured with SBAS InSAR method. *Environ. Earth Sci.* **72**, 677–691. <https://doi.org/10.1007/s12665-013-2990-y> (2014).
13. Bao, X. *et al.* Ground deformation pattern analysis and evolution prediction of Shanghai Pudong International Airport based on PSI long time series observations. *Remote Sens.* **14**, 610 (2022).
14. Fathian, A. *et al.* Complex co- and postseismic faulting of the 2017–2018 seismic sequence in western Iran revealed by InSAR and seismic data. *Remote Sens. Environ.* **253**, 112224. <https://doi.org/10.1016/j.rse.2020.112224> (2021).
15. Chen, Y. *et al.* Prediction of InSAR deformation time-series using a long short-term memory neural network. *Int. J. Remote Sens.* **42**, 6919–6942. <https://doi.org/10.1080/01431161.2021.1947540> (2021).
16. Qinghao, L. I. *et al.* Time series prediction method of large-scale surface subsidence based on deep learning. *Acta Geodaet. Cartogr. Sin.* **50**, 396–404. <https://doi.org/10.11947/j.AGCS.2021.20200038> (2021).
17. Fu, H., Shi, H., Xu, Y. & Shao, J. Research on gas outburst prediction model based on multiple strategy fusion improved snake optimization algorithm with temporal convolutional network. *IEEE Access* **10**, 117973–117984. <https://doi.org/10.1109/ACCESS.2022.3220765> (2022).
18. Aoqing, G. U. *et al.* N-BEATS deep learning method for landslide deformation monitoring and prediction based on InSAR: A case study of Xinpū landslide. *Acta Geodaet. Cartogr. Sin.* **51**, 2171–2182. <https://doi.org/10.11947/j.AGCS.2022.20220298> (2022).
19. Ma, F., Sui, L. & Lian, W. Prediction of mine subsidence based on InSAR technology and the LSTM algorithm: A case study of the Shigouyi Coalfield, Ningxia (China). *Remote Sens.* **15**, 2755 (2023).

20. Chen, B. *et al.* Time-varying surface deformation retrieval and prediction in closed mines through integration of SBAS InSAR measurements and LSTM algorithm. *Remote Sens.* **14**, 788 (2022).
21. Anantrasirichai, N., Biggs, J., Albino, F. & Bull, D. The application of convolutional neural networks to detect slow, sustained deformation in InSAR time series. *Geophys. Res. Lett.* **46**, 11850–11858 (2019).
22. Nukala, V. H., Nayak, M., Gubbi, J. & Purushothaman, B. *Image and Signal Processing for Remote Sensing XXVII* 154–159 (SPIE).
23. Chen, Y. *et al.* Prediction of InSAR deformation time-series using a long short-term memory neural network. *Int. J. Remote Sens.* **42**, 6919–6942 (2021).
24. Hill, P., Biggs, J., Ponce-Lopez, V. & Bull, D. Time-series prediction approaches to forecasting deformation in sentinel-1 InSAR data. *J. Geophys. Res. Solid Earth* **126**, e2020JB020176 (2021).
25. Kamran, M., Ullah, B., Ahmad, M. & Sabri, M. M. S. Application of KNN-based isometric mapping and fuzzy c-means algorithm to predict short-term rockburst risk in deep underground projects. *Front. Public Health* **10**, 1023890 (2022).
26. Kamran, M., Shahani, N. M. & Armaghani, D. J. Decision support system for underground coal pillar stability using unsupervised and supervised machine learning approaches. *Geomech. Eng.* **30**, 107 (2022).
27. Kamran, M., Chaudhry, W., Taiwo, B. O., Hosseini, S. & Rehman, H. Decision intelligence-based predictive modelling of hard rock pillar stability using K-nearest neighbour coupled with Grey Wolf optimization algorithm. *Processess* **12**, 783 (2024).
28. Kamran, M., Jiskani, I. M., Wang, Z. & Zhou, W. Decision intelligence-driven predictive modelling of air quality index in surface mining. *Eng. Appl. Artif. Intell.* **133**, 108399 (2024).
29. Deng, Z. *et al.* Land subsidence prediction in Beijing based on PS-InSAR technique and improved Grey-Markov model. *GISci. Remote Sens.* **54**, 797–818 (2017).
30. Fiorentini, N., Maboudi, M., Leandri, P., Losa, M. & Gerke, M. Surface motion prediction and mapping for road infrastructures management by PS-InSAR measurements and machine learning algorithms. *Remote Sens.* **12**, 3976 (2020).
31. Chen, Y., Tong, Y. & Tan, K. Coal mining deformation monitoring using SBAS-InSAR and offset tracking: A case study of Yu County, China. *IEEE J. Sel. Top. Appl. Earth Observ. Remote Sens.* **13**, 6077–6087. <https://doi.org/10.1109/JSTARS.2020.3028083> (2020).
32. Likas, A., Vlassis, N. & Verbeek, J. The global k-means clustering algorithm. *Pattern Recogn.* **36**, 451–461. [https://doi.org/10.1016/S0031-3203\(02\)00060-2](https://doi.org/10.1016/S0031-3203(02)00060-2) (2003).
33. Ikotun, A. M., Ezugwu, A. E., Abualigah, L., Abuhaija, B. & Heming, J. K-means clustering algorithms: A comprehensive review, variants analysis, and advances in the era of big data. *Inf. Sci.* **622**, 178–210. <https://doi.org/10.1016/j.ins.2022.11.139> (2023).
34. Likas, A., Vlassis, N. & Verbeek, J. J. The global k-means clustering algorithm. *Pattern Recogn.* **36**, 451–461 (2003).
35. Pham, D. T., Dimov, S. S. & Nguyen, C. D. Selection of K in K-means clustering. *Proc. Inst. Mech. Eng. C J. Mech. Eng. Sci.* **219**, 103–119 (2005).
36. Cui, M. *Introduction to the K-Means Clustering Algorithm Based on the Elbow Method* (2020).
37. Ahmed, M., Seraj, R. & Islam, S. M. S. The k-means algorithm: A comprehensive survey and performance evaluation. *Electronics* **9**, 1295 (2020).
38. Yu, Y., Si, X., Hu, C. & Zhang, J. A review of recurrent neural networks: LSTM cells and network architectures. *Neural Comput.* **31**, 1235–1270 (2019).
39. Dey, R. & Salem, F. M. *2017 IEEE 60th International Midwest Symposium on Circuits and Systems (MWSCAS)* 1597–1600 (IEEE).
40. Sherstinsky, A. Fundamentals of recurrent neural network (RNN) and long short-term memory (LSTM) network. *Phys. D Nonlinear Phenomena* **404**, 132306 (2020).
41. Hashim, F. A. & Hussien, A. G. Snake optimizer: A novel meta-heuristic optimization algorithm. *Knowl. Based Syst.* **242**, 108320. <https://doi.org/10.1016/j.knsys.2022.108320> (2022).
42. Li, Z., Du, Y. & Hu, Y. A method for predicting the morphology of single-track laser cladding layer based on SO-LSSVR. *Mater. Today Commun.* **39**, 108666. <https://doi.org/10.1016/j.mtcomm.2024.108666> (2024).
43. Zhou, Y., Huang, R., Lin, Q., Chai, Q. & Wang, W. Probabilistic optimization based adaptive neural network for short-term wind power forecasting with climate uncertainty. *Int. J. Electric. Power Energy Syst.* **157**, 109897. <https://doi.org/10.1016/j.ijepes.2024.109897> (2024).
44. Fu, R., Zhang, Z. & Li, L. *2016 31st Youth Academic Annual Conference of Chinese Association of Automation (YAC)* 324–328 (IEEE).
45. Fan, Y. & Sun, L. Satellite aerosol optical depth retrieval based on fully connected neural network (FCNN) and a combine algorithm of simplified aerosol retrieval algorithm and simplified and robust surface reflectance estimation (SREMARA). *IEEE J. Sel. Top. Appl. Earth Observ. Remote Sens.* **16**, 4947–4962 (2023).
46. Fan, Y., Sun, L. & Liu, X. GOCE-II geostationary satellite hourly aerosol optical depth obtained by data-driven methods: Validation and comparison. *Atmos. Environ.* **310**, 119965 (2023).
47. Fan, Y., Sun, L. & Liu, X. Data integration for ML-CNPM 2.5: A public sample dataset based on machine learning models and remote sensing technology applied for estimating ground-level PM 2.5 in China. *IEEE Trans. Geosci. Remote Sens.* **1**, 1 (2024).
48. Wu, H., Hayes, M. J., Weiss, A. & Hu, Q. An evaluation of the standardized precipitation index, the China-Z index and the statistical Z-score. *Int. J. Climatol.* **21**, 745 (2001).

Acknowledgements

The authors wish to thank the European Space Agency (ESA) for supplying the free Sentinel-1A SAR images.

Author contributions

Yixin Xiao: conceptualization, methodology, formal analysis, and writing-original draft. Qiuxiang Tao: conceptualization, methodology, funding acquisition, resources, supervision, validation, and writing-original draft and editing. Leyin Hu: conceptualization, supervision, methodology, and validation. Ruixiang Liu and Xuepeng Li: conceptualization and supervision. All authors contributed to the interpretation of the results and the writing of the paper. All authors have read and agreed to the published version of the manuscript.

Funding

This research was supported by the Shandong Natural Science Foundation under Grant No. ZR2020MD044; the National Natural Science Foundation of China under Grant No. 42974009; Shandong Province Higher Education Research Development Plan Project under Grant No. J18KB091.

Competing interests

The authors declare no competing interests.

Additional information

Correspondence and requests for materials should be addressed to Q.T.

Reprints and permissions information is available at www.nature.com/reprints.

Publisher's note Springer Nature remains neutral with regard to jurisdictional claims in published maps and institutional affiliations.

Open Access This article is licensed under a Creative Commons Attribution-NonCommercial-NoDerivatives 4.0 International License, which permits any non-commercial use, sharing, distribution and reproduction in any medium or format, as long as you give appropriate credit to the original author(s) and the source, provide a link to the Creative Commons licence, and indicate if you modified the licensed material. You do not have permission under this licence to share adapted material derived from this article or parts of it. The images or other third party material in this article are included in the article's Creative Commons licence, unless indicated otherwise in a credit line to the material. If material is not included in the article's Creative Commons licence and your intended use is not permitted by statutory regulation or exceeds the permitted use, you will need to obtain permission directly from the copyright holder. To view a copy of this licence, visit <http://creativecommons.org/licenses/by-nc-nd/4.0/>.

© The Author(s) 2024